Novel chitosan based metal-organic polyhedrons/enzyme hybrid hydrogel with antibacterial activity to promote wound healing

Jie Song, Chaoqun Zhang, Shaowen Kong, Fangyu Liu, Wenju Hu, Feng Su, Suming Li

Novel chitosan based metal-organic polyhedrons/enzyme hybrid hydrogel with antibacterial activity to promote wound healing

Jie Song [a,1], Chaoqun Zhang [a,1], Shaowen Kong [a], Fangyu Liu [a], Wenju Hu [a], Feng Su [a,b,*], Suming Li [c,**]

[a] State Key Laboratory Base of Eco-chemical Engineering, College of Chemical Engineering, Qingdao University of Science and Technology, Qingdao 266042, China
[b] Institute of High Performance Polymers, Qingdao University of Science and Technology, Qingdao 266042, China
[c] Institut Europeen des Membranes, UMR CNRS 5635, Universite de Montpellier, 34095 Montpellier, France

ARTICLE INFO

Keywords:
Metal-organic polyhedrons
Glucose oxidase
Chitosan
Hybrid hydrogel
Antibacterial activity
Wound healing

ABSTRACT

This work aimed to develop a novel chitosan based metal-organic polyhedrons (MOPs)/enzyme hybrid hydrogel with superior antimicrobial properties in wound healing treatment. Hybrid hydrogel was prepared by crosslinking glucose oxidase (GOx), vanadium metal-organic polyhedrons (VMOP-2) and chitosan using glutaraldehyde as crosslinker. The formed GVCS hydrogel was characterized by using various techniques, including FTIR, SEM, XPS, TGA and EDX. Data show that GVCS hydrogel was successfully obtained with uniform distribution of GOx and VMOP-2 in the hydrogel structure. Antibacterial tests show that GVCS hydrogel exhibits better bactericidal effect on both gram-negative bacteria (*S. aureus*) and gram-positive bacteria (*E. coli*) compared to other hydrogel samples because of its hydroxyl radicals generation capacity in the presence of glucose. MTT assay shows that the hydrogel presents good cell compatibility. *In vivo* experiments using an infected wound model indicate that GVCS hydrogel can effectively facilitate wound healing. Therefore, chitosan based MOPs/enzyme hybrid hydrogel could be most promising for antibacterial therapy in clinical applications.

1. Introduction

Wound healing is the inherent ability of biological tissues to self-repair after injury. However, serious complications could occur in case of infections caused by bacteria such as *Escherichia coli* (*E. coli*) and *Staphylococcus aureus* (*S. aureus*). Wound infection triggers the body's immune response, provokes inflammation, slows the healing process, and even requires medical intervention (He et al., 2020), resulting in increased healthcare costs (Xiao et al., 2017). If not treated in time, the infection could worsen and even lead to sepsis (Qu et al., 2019). Therefore, novel multifunctional wound dressing materials need to be developed for wound care in surgery, trauma emergency, and even battlefield rescue (Guidolin & Zheng, 2019).

Tremendous efforts have been dedicated to developing three-dimensional bioengineered substitutes, including films, sponges, hydrogels and nanofibers (Bayer, 2021; Wang et al., 2009). Chitosan (CS), the only alkaline polysaccharide, has been widely investigated for applications in the biomedical fields (Zhang et al., 2011). Chitosan based hydrogels present good cytocompatibility (Bhattarai et al., 2010), and could accelerate wound healing (Patrulea et al., 2015). The antibacterial effect of chitosan based hydrogel results from its cationic amino groups that damage the bacterial membrane and disrupts the mass transport across the bacterial wall (Wu et al., 2014). This single antibacterial function leads to limited antibacterial effect. Therefore, it becomes a challenging issue to develop novel composite hydrogels with multiple antibacterial mechanisms for wound infection treatment.

Metal-organic polyhedrons (MOPs) as the subunits of metal-organic frameworks (MOFs), have unique properties such as ordered structure (Eddaoudi et al., 2001), specific cavities (Li & Zhou, 2010), tunable pore size (Kang et al., 2016), good stability (Carné-Sánchez et al., 2019), and modification sites (Lu et al., 2011). MOPs also present excellent processability due to their solubility in certain solvents (Carné-Sánchez et al., 2018). These properties enable facile formulation of MOPs containing hybrid materials. Qin et al. synthesized a copper-MOP hydrogel

* Correspondence to: F. Su, State Key Laboratory Base of Eco-chemical Engineering, College of Chemical Engineering, Qingdao University of Science and Technology, Qingdao 266042, China.
** Corresponding author.
E-mail addresses: sufeng@qust.edu.cn (F. Su), suming.li@umontpellier.fr (S. Li).
[1] Authors equally contributed to this work and are both co-first authors.

which exhibited excellent antibacterial activity (Qin et al., 2019); Chen et al. reported a PAA-Cu-MOP hydrogel which could accelerate wound healing (Chen et al., 2020). However, no studies have been reported exploring MOPs/biopolymer hybrid hydrogels as wound healing materials. It is thus of great interest to investigate such hybrid hydrogels to improve the antibacterial properties and treatment effect (de Lima et al., 2021).

Glucose oxidase (GOx) is an oxidoreductase which catalyzes glucose oxidation to gluconic acid and hydrogen peroxide (H_2O_2). GOx has been used to control wound infection as H_2O_2 can inhibit bacterial growth (Peng et al., 2022). However, the antibacterial activity of H_2O_2 is lower than that of •OH radicals (Li et al., 2021). Mimetic enzyme materials such as iron oxide (Gong et al., 2020), vanadium pentoxide (V_2O_5) (Natalio et al., 2012), and graphene quantum dots (Sun et al., 2014) have been used to convert H_2O_2 into more toxic •OH radicals, which could dramatically enhance the antibacterial effect. Interestingly, MOPs appear as an ideal mimetic enzyme material due to their abundant metal sites and good physical properties. Combination of MOPs and GOx could be very efficient to generate •OH radicals for uses in wound infection treatment.

This work aimed to synthesize a peroxidase-like GOx/VMOP-2/CS (GVCS) hybrid hydrogel with superior antibacterial and wound healing promoting properties. As depicted in Scheme 1, GVCS hydrogel was prepared by crosslinking GOx, VMOP-2 and chitosan using glutaraldehyde as crosslinker. GOx could convert glucose to gluconic acid and H_2O_2, and VMOP-2 could convert H_2O_2 to ·OH radicals. Thus GVCS hydrogel could exhibit better antibacterial activity than CS hydrogel on both gram-negative bacteria (*S. aureus*) and gram-positive bacteria (*E. coli*). Antibacterial and wound healing experiments were performed to evaluate the potential of GVCS hydrogel in wound infection treatment applications.

2. Materials and methods

2.1. Materials and reagents

2-Aminoterephthalic acid (98%), vanadium (III) chloride (VCl_3) (99%), glucose oxidase (from Aspergillus Niger, >180 U/mg) and horseradish peroxidase (HRP) (>200 U/mg) were obtained from Mucklin (Shanghai, China). Glutaraldehyde (25% solution) and chitosan (Mw 600 KDa, deacetylation degree ≥90%, from shrimp and crab shells) were supplied by Aladdin (Shanghai, China). Fluorescein isothiocyanate (FITC, ≥90%) and 3,3′,5,5′-tetramethylbenzidine dihydrochloride (TMB·2HCl, ≥98.0%) were supplied by Solarbio (Beijing, China). TNF-α rabbit polyclonal antibodies (pAbs) and VEGF rabbit polyclonal antibodies (pAbs) were purchased from ABclonal (Wuhan, China). All other solvents were of analytical grade and used as received.

2.2. Synthesis of materials

2.2.1. Synthesis of VMOP-2

VMOP-2 was synthesized according to the literature method (Zhang et al., 2016b). 2-Aminoterephthalic acid (20 mg, 0.11 mmol) and VCl_3 (30 mg, 0.19 mmol) were added into a mixture of 2 mL DMF and 0.5 mL ethanol, and dissolved *via* ultrasound. Then the mixture was placed in a Teflon-lined stainless-steel vessel. The reaction proceeded at 150 °C for 48 h. After cooling down to room temperature, dark green crystals were obtained. The crystals were thoroughly washed with ethanol and air dried.

2.2.2. Preparation of hydrogels

Hydrogel preparation refers to a literature method with modifications (Martínez-Mejía et al., 2019). Firstly, 0.2 g chitosan was dissolved in 10 mL acetic acid (1 wt%). 2 mL GOx (1 mg/mL) and 2 mL VMOP-2 (2 mg/mL) aqueous solutions were then dropped in chitosan solution and homogenized, followed by addition of 5 mL glutaraldehyde solution (1 wt%). The mixture was stirred for 30 min, and placed at 37 °C for 12 h. The resulted GVCS hydrogel was washed with deionized water 3 times and freeze-dried. CS, VMOP-2-CS (VCS), and GOx-CS (GCS) hydrogels were prepared as control following the same procedure.

2.3. Swelling of hydrogels

Freeze dried GVCS and CS hydrogels (200 μL) were immersed in 5 mL pH 7.4 phosphate buffered saline (PBS) at 37 °C. At various time intervals, the swollen samples were recovered, blotted with paper to remove surface water, and weighed. Finally the hydrogels were freeze dried and weighed again.

The swelling and weight loss ratios were calculated using the following equations:

$$\text{Swelling ratio } (\%) = ((W_s - W_d)/W_d)*100 \quad (1)$$

$$\text{Weight loss } (\%) = ((W_0 - W_d)/W_0)*100 \quad (2)$$

where W_s is the wet weight of swollen hydrogel, W_d the dried weight and W_0 is the initial weight.

2.4. Characterization

X-ray diffraction (XRD) patterns were recorded in the range from 5 to 50° on a Rigaku d_{max} 2500 diffractometer using Cu Kα (λ = 1.5418 Å) radiation, at a scan speed of 1 s/step.

Fourier transform infrared (FT-IR) spectra were obtained on a Nicolet-IS50 FT-IR spectrometer using KBr pellets, from 500 to 4000

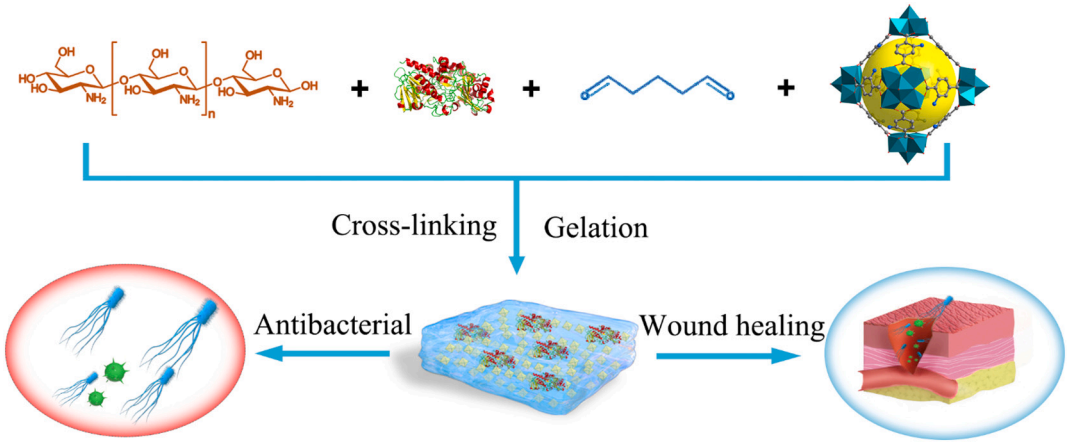

Scheme 1. Schematic description of GVCS hydrogel preparation and its antibacterial and wound healing effect.

cm^{-1}, 32 scans at a resolution of 4 cm^{-1}.

UV–Vis absorption spectra were recorded using Perkin Elmer (Lambda 950) UV–visible spectrometer.

Dynamic light scattering (DLS) was performed on a BI-200SM (Brookhaven Instruments Corporation) with a He-Ne laser ($\lambda = 633$ nm).

X-ray photoelectron spectroscopy (XPS) was performed on Escalab 250Xi (Thermo Fisher Scientific) using Al as excitation source.

Scanning electron microscopy (SEM) was realized using JSM-7610F filed-emission SEM. Freeze-dried hydrogels were cut into small pieces, gold-coated and observed at 50× magnification using an electron beam at accelerating voltage of 3 kV.

Energy dispersive X-ray analysis (EDX) spectra were registered using JSM-7610F filed-emission SEM under an electron beam acceleration voltage of 15.0 kV.

Thermogravimetric analysis (TGA) was performed using a TG 209 F3 (Netzsch) under nitrogen atmosphere at a heating rate of 10 °C min^{-1} up to 800 °C.

The rheological properties of hydrogels were determined using a TA rheometer (DHR-2). The storage modulus (G′) and loss modulus (G″) were measured by performing a frequency sweep (0.01–10 Hz). The apparent viscosity of hydrogels was monitored as a function of shear rate (0.01–100 s^{-1}) (Wang et al., 2019).

The compressive strength of cylindrical hydrogel samples (diameter 1.5 cm, height 1 cm) was determined using TA Instruments Q800 series at strain rate of 1 mm/s^{-1} (Yang et al., 2020).

2.5. Peroxidase mimetic activity and detection of hydroxyl radical (•OH)

2.5.1. Peroxidase mimetic activity

300 μL TMB·2HCl (10 mM), 45 μL glucose (1 wt%) were dissolved in PBS (0.1 M, pH = 7.4) to a final volume of 3 mL. 5 mg GVCS dried hydrogel was added and incubated at room temperature for 30 min. The peroxidase-like activity was monitored at 652 nm using UV–vis spectrophotometry.

2.5.2. Detection of hydroxyl radical (•OH)

The generation of •OH was evaluated by monitoring the fluorescence change of 2-hydroxy terephthalic acid (TAOH) due to the oxidation of terephthalic acid (TA).

Several groups were prepared for reaction in PBS (pH = 7.4, 50 mM), including TA; TA and H_2O_2; TA and VMOP-2; TA, GVCS hydrogel and glucose; TA, VMOP-2 and H_2O_2; TA, CS hydrogel and glucose. The concentration of TA, H_2O_2, glucose and VMOP-2 was 0.5 mM, 1 mM, 1 wt% and 50 μg/mL, respectively. Reaction occurred for 12 h in the dark. The fluorescence intensity was measured at 435 nm.

2.5.3. Enzyme activity of free GOx and GCS

The enzyme activity was determined at 25 °C with PBS buffer (pH = 7.4) using Perkin Elmer (Lambda 950) UV–visible spectrometer. Catalysis was carried out in 3 mL PBS buffer containing TMB·2HCl (10 mM, 300 μL), glucose (1 wt%, 300 μL), HRP and GOx (1 mg/mL, 31 μL) or GCS hydrogel (2 mg). The enzyme concentration in both GOx and GCS groups was 10 μg/mL. The concentration of oxidized TMB was calculated from Beer-Lmbert Law using a molar absorption coefficient of 39,000 M^{-1} cm^{-1} (Liu et al., 2014). The catalysis rate was determined from the average rates of the first 3 min.

2.6. Bacterial culture and antimicrobial test

LB agar medium was prepared as follows: 10 g tryptone, 5 g yeast extract, 10 g NaCl and 15 g agar were dissolved in 1 L PBS (pH = 7.2), and autoclaved at 120 °C for 20 min. Monoclonal bacteria on the solid LB agar medium were transferred to 10 mL liquid LB medium, and cultured at 37 °C at 175 rpm for 12 h. When reaching the logarithmic growth period, the bacterial solution was diluted to 10^6 CFU/mL with PBS (Zhang et al., 2021).

For solid medium culture, 50 μL of the diluted bacteria solution and 50 μL glucose (4.0 mM) were streaked on the solid LB agar medium. The concentration of glucose was within the normal range of glucose concentration in body (Reddy et al., 2018). After streaking, the CS, GCS, VCS and GVCS hydrogels were placed separately in *E. coli*- or *S. aureus*-cultured plates, and cultured at 37 °C to evaluate the inhibition zone (Ou et al., 2020).

For the growth-inhibition assay, 100 μL bacterial suspension at a density of 10^7 CFU/mL was added in open wells containing 1 mL PBS, followed by addition of hydrogels. Incubation then proceeded at 37 °C for 48 h to assess colonies growth. Bacterial concentration was determined by absorbance measurements at 600 nm (Tao et al., 2019).

2.7. Cytotoxicity test

The cytotoxicity of hydrogels was evaluated by MTT assay on L929 cell line. CS and GVCS hydrogels were immersed in 5 mL serum-containing medium and incubated at 37 °C for 24 h. 100 μL of L929 cells (2×10^4 cells per mL) were seeded in 96-well plates and incubated for 24 h. Then, 100 μL medium incubated with GVCS hydrogel was added to replace the original medium. The cells viability was determined using MTT assay.

Live-dead cells staining was done by acridine orange/propidium iodide (AO/PI) double staining kit (Beijing Biolab Technology Co., Ltd.). L929 cells with a density of 10^5 cells per well were cultured in a 6-well plate for 12 h to allow cells attachment. Afterwards, cells were washed twice with PBS (10 mM, pH 7.4), and hydrogel samples (200 μg/mL) were added. After 24 h incubation, the cell culture medium was discarded and washed with PBS (10 mM, pH 7.4). Then 200 μL fresh medium containing 5 μL AO and 10 μL PI was added. After 20 min culture in the dark at 4 °C, the cells were washed with PBS and imaged by using inverted fluorescence microscope.

2.8. In vivo tests

2.8.1. Mouse model establishment

All animal experiments were performed in accordance with the guidelines of the National Research Council's Guide for the Care and Use of Laboratory Animals. To evaluate the *in vivo* antibacterial and wound healing promoting properties of GVCS hydrogel, a wound model was realized on the back of male Kunming mice (30–34 g, 7 weeks old). The *S. aureus* strain was inoculated in LB liquid medium and shaken for 12 h at 37 °C. Then, the bacteria were resuspended in PBS and diluted to 10^8 CFU/mL. The mice were slashed with a wound of about 25 mm^2 on which 50 μL of *S. aureus* suspension were dropped. After 24 h, the infected mice were treated with PBS, CS or GVCS hydrogels. Both hydrogels were previously treated by immersion in pH = 7.4 PBS for 12 h. Wound healing was examined after 3, 7, 10, 15, and 25 days. The wound area was recorded with a camera and calculated with image processing software (Image J) according to the following formula:

$$\text{Wound area } (\%) = ((A_0 - A_t)/A_0)*100 \quad (3)$$

where A_0 is the original wound area, and A_t is the wound area at the time of examination.

2.8.2. Wound bacteria content, histology and immunohistochemistry

The tissues recovered at 25th day were excised and incubated in sterile saline at 37 °C for 12 h. Then, the culture solution was diluted 10^3-fold, and cultured on LB agar plates at 37 °C for 24 h. Finally the number of bacterial colonies was counted (Hu et al., 2020).

Hematoxylin-Eosin (H&E) and Masson's trichrome staining was conducted for histomorphological analysis of wound regeneration. Rat epithelial tissue samples collected at 25th day were fixed with 4% (w/v) paraformaldehyde, dehydrated, and embedded in paraffin. Each sample was cut into 5 μm thickness slices (Yao et al., 2021), stained with H&E

(Beyotime, China), analyzed and photo-captured by microscope (IX53, Olympus, Japan).

Immunohistochemistry of paraffin-embedded histological sections was tested using TNF-α rabbit pAb and VEGF rabbit pAbs at a dilution of 1:100 (40×). High-pressure antigen retrieval was previously performed using 10 mM citrate buffer pH 6.0.

2.9. Statistical analysis

Multi-sample data are described by the mean ± standard deviation (SD), and data analysis was performed using Graphpad software 8.0. All muti-sample data were analyzed by ANOVA. Statistically significant difference between them was set as $p < 0.05$.

3. Results and discussion

3.1. Characterization of VMOP-2

The structure of VMOP-2 is schematically shown in Fig. 1a. VMOP-2 crystals exhibit an octahedron structure with a size of about 50 μm (Fig. 1b). The XRD pattern of VMOP-2 is shown in Fig. 1c, in comparison with the calculated pattern. VMOP-2 exhibits high crystallinity with the same crystalline structure as the calculated pattern (Zhang et al., 2016b). FT-IR spectrum of VMOP-2 shows various characteristic signals (Fig. 1d), especially those at 3437 cm^{-1} and 3340 cm^{-1} corresponding to the stretching of O—H and N—H, at 2962 cm^{-1} to the stretching of C—H, at 1253 cm^{-1} to the stretching of C—O bond, and at 1535 cm^{-1} and 1381 cm^{-1} to the stretching of double carbon bonds of benzene ring (Zhang et al., 2016a). TGA reveals the good thermal stability of VMOP-2 (Fig. 1e). A weight loss of 20.8% is observed from 50 to 390 °C, corresponding to the loss of DMF molecules and $[NH_2Me_2]^+$ cations. Weight loss beyond 390 °C results from the cage framework decomposition (Zhang et al., 2016a).

XPS survey spectrum shows that VMOP-2 was composed of C 1s, N 1s, O 1s, V 2s, and V 2p (Fig. 1f). The XPS spectrum of C 1s (Fig. 1g) displays three major peaks at 284.60, 286.01 and 288.62 eV, corresponding to C—C, C—(O,N) and C═O, respectively (Ming et al., 2019). The binding energy of 515.06 (V^{IV}), 516.13 (V^{V}) and 527.73 eV (V—O) indicates the structure of $\{V_5O_9Cl\}$ clusters in VMOP-2, as shown in Fig. 1h (Biesinger et al., 2010). Fig. 1i presents the O1s spectrum of VMOP-2. The binding energy of 530.63, 532.00 and 533.56 eV well corroborates with the structure of V—O, O═C—O, and C—O species (Xue et al., 2018). All these data indicate the successful synthesis of VMOP-2.

It is known that VMOP-2 is dispersed in aqueous medium in the form of nano-cages. The dispersion performance of VMOP-2 was confirmed by DLS measurements (Bae et al., 2017). An average size of 1.5 nm is obtained with a polydispersity index of 0.107 (Fig. S1a), which corroborates with the TEM image (Fig. S2). The zeta potential of VMOP-2 is −16.4 mV. (Fig. S1b). These results demonstrate the homogeneity of VMOP-2 nano-cages, which can be uniformly dispersed to prepare composite materials.

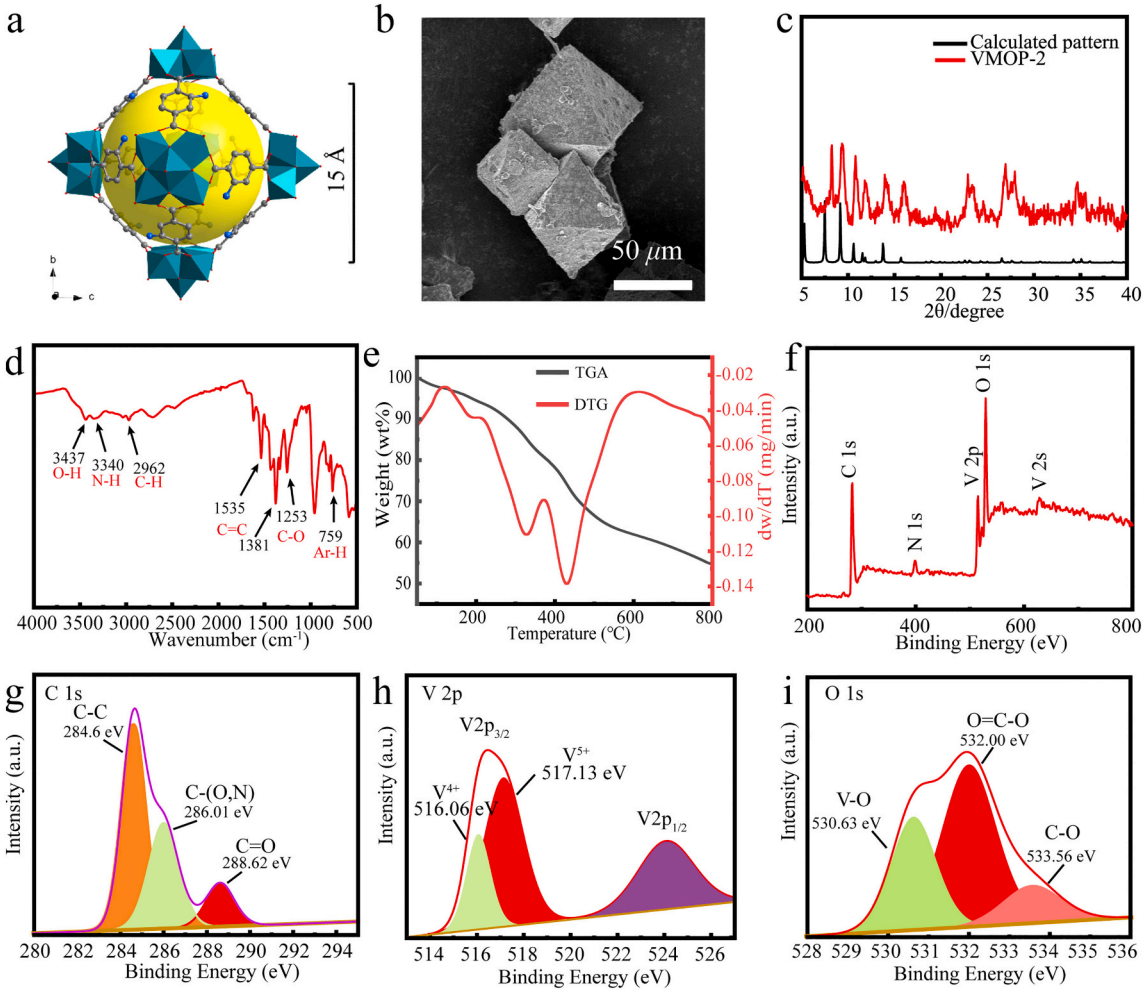

Fig. 1. Characterization of VMOP-2: (a) cage structure of VMOP-2; (b) SEM image of VMOP-2; (c) XRD pattern of VMOP-2; (d) Infrared spectra of VMOP-2; (e) TGA and DTG thermograms of VMOP-2; (f–i) XPS survey spectrum and high-resolution C 1s, V 2p, and O 1s spectra of VMOP-2.

3.2. Characterization of GVCS hydrogel

The chemical structure of GVCS hydrogel is verified by FT-IR (Fig. 2a). The broad peak around 3300 cm^{-1} is assigned to O—H stretching and N—H stretch. The peaks at 2931 cm^{-1} and 2869 cm^{-1} belong to asymmetric and symmetric stretching vibration of —CH_2 group (Cui et al., 2018), and peaks at 1646 and 1558 cm^{-1} to amide I, amide II as well as NH_2 bending, respectively (Dudek et al., 2020). The intensity of peaks at 1646 cm^{-1} (amide I) and 1033 cm^{-1} (C—OH) increased compared to CS hydrogel. This difference is assigned to the formation of imine bonds by crosslinking between aldehyde groups of glutaraldehyde and amino groups of chitosan, VMOP-2 and GOx. SEM image of freeze dried hydrogel shows a honeycomb structure (Fig. 2b). There is little difference between the SEM images of CS (Fig. S3) and GVCS hydrogels, suggesting that addition of GOx and VMOP-2 has little influence on hydrogel morphology.

XPS survey spectrum shows that GVCS hydrogel is composed of C, N, O, S, V elements (Fig. 2c). Fig. 2d shows three peaks of C 1s at 284.6, 286.04, and 287.69 eV, corresponding to C—C, C—(O,N), and C═O bonds, respectively. Fig. 2e shows two peaks of N 1s at 399.42 and 402.25 eV corresponding to N—C═O and N—H, respectively. XPS results confirm the crosslinking structure of GVCS hydrogels, in agreement with FT-IR spectra.

The thermal stability of GVCS and CS hydrogel were evaluated by TGA under nitrogen atmosphere (Fig. 2f). Weight loss below 110 °C (5.1% for GVCS and 6.1% for CS hydrogel) is attributed to the removal of free water, and that between 110 and 210 °C (7.2% for GVCS and 8.3% for CS hydrogel) to the removal of bound water and beginning of shorter chains decomposition. The second weight loss of hydrogels begins at about 210 °C. Weight loss between 210 and 450 °C is related to the degradation of chitosan (45.0% for GVCS and 48.3% for CS hydrogel) (Nematidil et al., 2019). The weight loss beyond 390 °C of GVCS hydrogel also includes the decomposition of VMOP-2 according to TGA data of VMOP-2. The residual weights of GVCS and CS hydrogel are 32.7% and 28.6%, respectively. The weight loss of GVCS hydrogel is lower than that of CS hydrogel. The improved thermal stability is consistent with the enhanced crosslinking of GVCS hydrogel by VMOP-2.

EDX elemental mapping is performed to confirm the successful doping of GOx and VMOP-2. Fig. 2g shows that C, S and V elements are uniformly dispersed, thus demonstrating the uniform distribution of GOx and VMOP-2 in the hydrogel structure. FITC was used to label GOx to further observe GOx distribution in GVCS hydrogel. As shown in Fig. S4, fluorescence microscopy images also confirm the uniform distribution of GOx.

3.3. Swelling of hydrogels

Wound healing can be delayed by the exudates and maceration of uninjured skin around the wound. Thus, hydrogels for wound healing uses should have suitable swelling capacity for absorbing exudates. The swelling behaviors of CS and GVCS were followed up to 48 h. As shown in Fig. 3a, a swelling equilibrium is reached beyond 10 h. The swelling ratio of GVCS hydrogel (*c.a* 70%) is slightly lower than that of CS hydrogel (*c.a* 80%), which might be attributed to the fact that VMOP-2 enhanced the structure of hydrogel. MOP particles, which has high

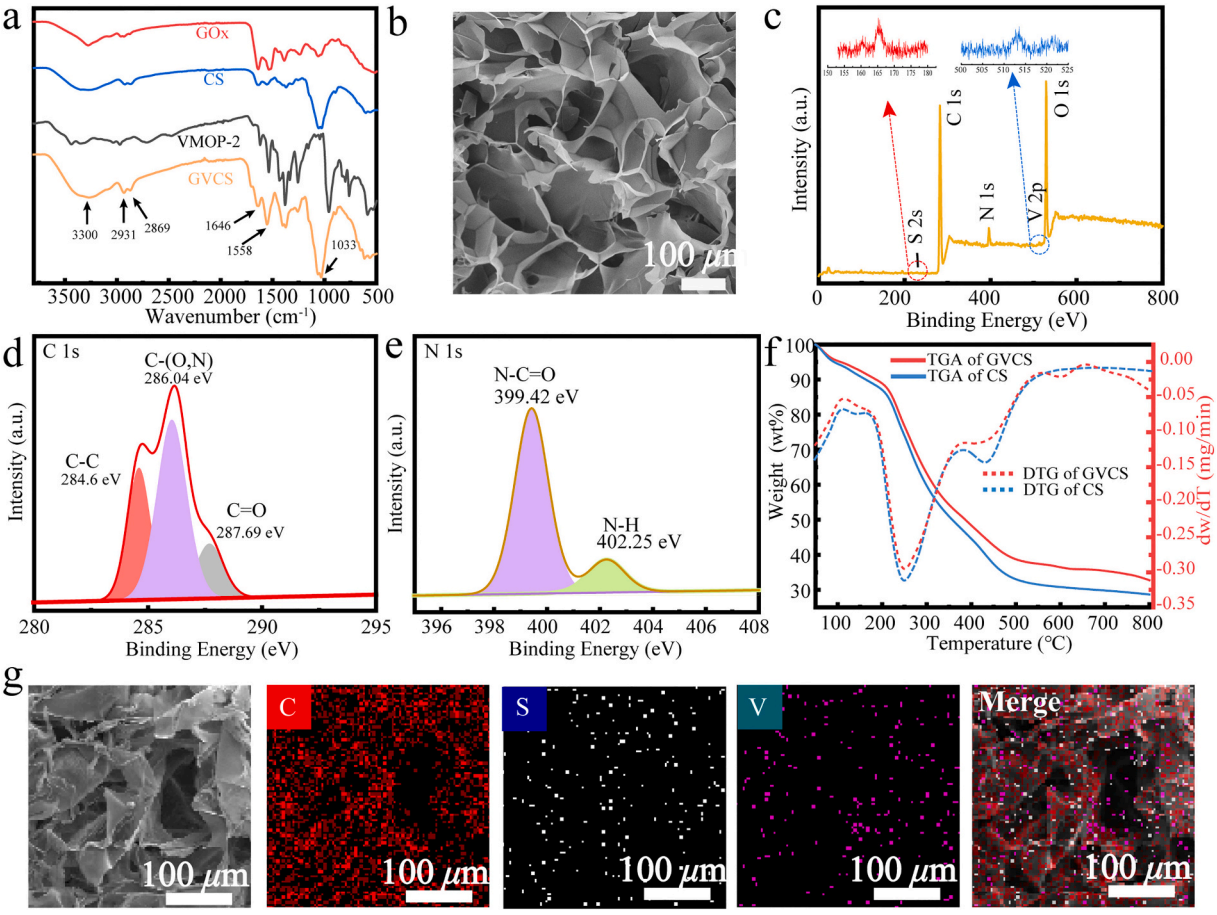

Fig. 2. Characterization of GVCS hydrogel: (a) Infrared spectra of GVCS hydrogel, VMOP-2, CS and GOx; (b) SEM image of freeze dried GVCS hydrogel; (c–e) XPS survey spectrum and high-resolution spectra of C 1s and N 1s of GVCS hydrogel; (f) TGA and DTG patterns of freeze-dried CS and GVCS hydrogels; (g) SEM-EDX of GVCS hydrogel.

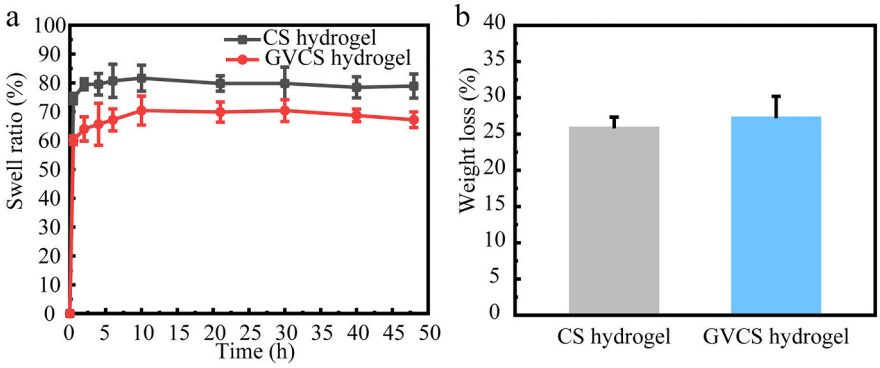

Fig. 3. (a) Swelling ratio changes and (b) weight loss percentage of GVCS and CS hydrogels during 48 h swelling.

connectivity, might improve the crosslinking and stabilize the gel network, thus leading to lower swelling of hydrogels (Liu et al., 2018). Fig. 3b shows the weight loss of GVCS and CS hydrogels after swelling. A weight loss of 27% is obtained for GVCS, which is slightly higher than that of CS hydrogel (26%). The weight loss mainly results from the washing away of uncrosslinked species. The swelling behavior and equilibrium water content (EWC) indicate that GVCS hydrogel can provide an appropriate microenvironment able to promptly absorb exudates and maceration of wound.

3.4. Mechanical properties of hydrogels

The rheological properties of hydrogels were measured at 25 °C. Variation of storage modulus (G′) and loss modulus (G″) with frequency is shown in Fig. S5a. In all frequency range (0.1 Hz–10 Hz), G″ is much smaller than G′, indicating a strong hydrogel structure. Little difference is observed between CS and GVCS hydrogels. Fig. S5b shows apparent viscosity *vs.* shear rate curves of hydrogels. The viscosity of hydrogels decreases with increasing shear rate, indicating a shear-thinning behavior. The viscosity of GVCS hydrogel is higher than CS hydrogel probably due to the covalent cross-linking of VMOP-2, GOx and chitosan (Liu et al., 2018).

The compressive strength of GVCS hydrogel is higher than that of CS hydrogel as shown in Fig. S6. This finding could be explained by the presence of VMOP-2 which serves as rigid attachment sites to enhance the strength. Meanwhile, adhesion experiments prove that GVCS hydrogel has good adhesive property (Fig. S7). GVCS hydrogel can adhere to skin, metal, glass and plastic surfaces, and has a certain degree of ductility.

3.5. Peroxidase-like activity and radicals detection

Many vanadium oxides such as VOx nanoflakes (Zeb et al., 2016) and V_2O_5 nanoparticles (Huang et al., 2019) possess peroxidase-like activity. Therefore, the $\{V_5O_9Cl\}$ cluster of VMOP-2 is expected to exhibit peroxidase-like activity and generate ·OH radicals in the presence of H_2O_2. The peroxidase-like activity of VMOP-2 and GVCS hydrogel was determined *via* UV–vis spectroscopy by detecting oxidized TMB which

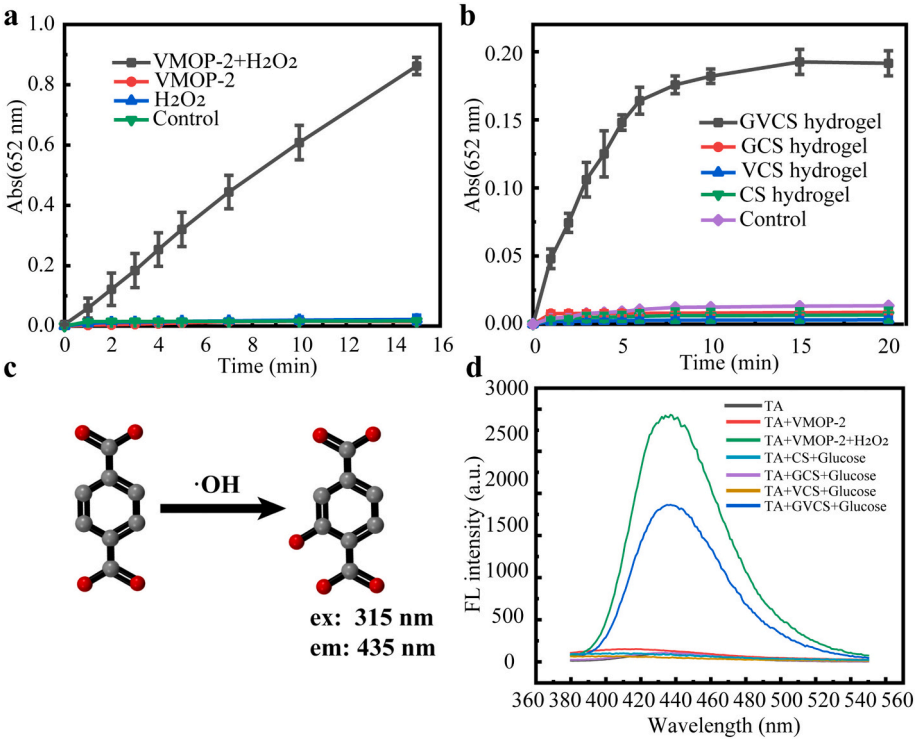

Fig. 4. Peroxidase-like activity of VMOP-2 (a) and GVCS hydrogel (b); Schematic diagram of fluorescence detection of •OH radicals (c); Fluorescence spectra result of •OH radical detection (d).

has an absorbance maximum at 652 nm (Wang, Peng, et al., 2021; Wang, Zhou, et al., 2021). As shown in Fig. 4a–b, a constant increase in absorbance is observed for VMOP-2 and GVCS groups, whereas the absorbance remains almost unchanged for controls. The catalytic activities of free GOx and GCS hydrogel are compared to elucidate the influence of immobilization on enzyme activity. As shown in Fig. S8a, free GOx shows higher catalysis rate (1.99 μM/min) than GCS hydrogel (0.92 μM/min). Although GOx immobilized in hydrogel retains only 46% activity (Fig. S8b), the reduced activity could avoid skin irritation due to large amounts of H_2O_2.

To further analyze the generation of ·OH radicals, TA was used as a •OH capturing probe (Zhang et al., 2021) (Fig. 4c–d). Fig. 4d depicts the fluorescence patterns of CS, GCS, VCS, GVCS and VMOP-2 groups after 12 h reaction. OH radicals are detected for GVCS hydrogels and VMOP-2 groups only, showing that peroxidase-like VMOP-2 could convert H_2O_2 into •OH radicals. It could be concluded that the peroxidase-like activity of VMOP-2 was derived from their ability to convert H_2O_2 into •OH radicals.

3.6. Antimicrobial property of GVCS hydrogel

Gram-positive bacteria (*E. coli*) and gram-negative bacteria (*S. aureus*) were used as model bacterium to evaluate the antibacterial effect of hydrogels. As shown in Fig. 5a, all hydrogels exhibit antibacterial activity against *E. coli* and *S. aureus* in the presence of glucose. GVCS exhibits relatively longer antibacterial time than other hydrogels. Moreover, the inhibition zone becomes smaller after 24 h in CS, VCS and GCS groups. VCS has the lowest antibacterial activity probably due to fewer amino groups after crosslinking. The inhibition zone of GVCS is much larger than that of other hydrogels (Fig. 5b–c). The sustained antibacterial activity assay also proved that GVCS has long-acting antibacterial activity in the presence of glucose (Fig. 5d–e). These findings could be attributed to the fact that GOx and VMOP-2 continuously generate ·OH radicals, leading to high antibacterial activity without toxicity from H_2O_2. A number of MOPs/MOFs hybrid hydrogels with different antibacterial mechanisms are summarized in Table S1. Compared with other hydrogels, the antibacterial activity of GVCS only requires glucose, thus avoiding extra addition of H_2O_2 or toxicity of metallic ions. Besides, the generation rate of •OH radicals varies as a function of glucose concentration around the wound, thus preventing strong and constant stimulation of radicals to wound tissue.

3.7. Cytotoxicity test

The biocompatibility of biomaterials is of crucial importance in biomedical applications (Cai et al., 2018). The cytotoxicity of VMOP-2 and GVCS hydrogel was evaluated by MTT assay after 48 h incubation with L929 cells. As shown in Fig. 6a–b, VMOP-2 and GVCS hydrogel present good biocompatibility. The cell viability is above 78% for VMOP-2 in the range of 1–5 μM, although a slight decrease is observed beyond 3 μM. In the case of GVCS hydrogel, the cell viability is well above 88% in the range of 20–200 μg/mL.

VMOP-2, GVCS and CS samples were incubated with L929 cells for 24 h, and then all cells were stained with AO/PI kit. No apoptosis is observed for cells incubated with CS and GVCS hydrogels as in the case of control, in contrast to VMOP-2 group. These findings could be attributed to the fact that GVCS hydrogel could limit the diffusion radius of •OH radicals (Wang, Peng, et al., 2021; Wang, Zhou, et al., 2021). With the decrease of glucose during wound healing, the hydrogel could reduce ·OH radical production and avoid irritation to the wound. According to the United States Pharmacopoeia Standards, it is concluded that GVCS hydrogel has outstanding biocompatibility and is suitable for uses as wound dressing.

3.8. Mouse model studies

A full-thickness infected wound model was established by creating wounds of about 25 mm^2 on mice back. The mice were randomly divided in three groups, and treated with PBS (control group), CS and GVCS hydrogels, respectively. The wounds were examined after healing (Fig. 7a–b). Generally, the wounds were nearly healed after 15 days in the GVCS group, while slower healing was observed in the control and CS groups (Fig. 7c). In fact, significant difference between CS and GVCS groups is observed from the seventh day. The number of surviving bacteria in wound tissues after 14 days is shown in Fig. 7d–e. The wound tissue of GVCS group presents the lowest bacterial content (9.87 10^4·CFU/mL), which is significantly lower than those of the control group (5.87 10^6·CFU/mL) and the CS group (7.31 10^5·CFU/mL). Therefore, GVCS hydrogel could promote wound healing *in vivo* owing to the antimicrobial activity of •OH radicals generated by GVCS hydrogel using glucose of the wound.

To further analyze the wound-healing efficiency, H&E and Masson's trichrome staining was employed for histological analysis of skin tissues after 25 days treatment (Xiao et al., 2017). In H&E staining (Fig. 8a),

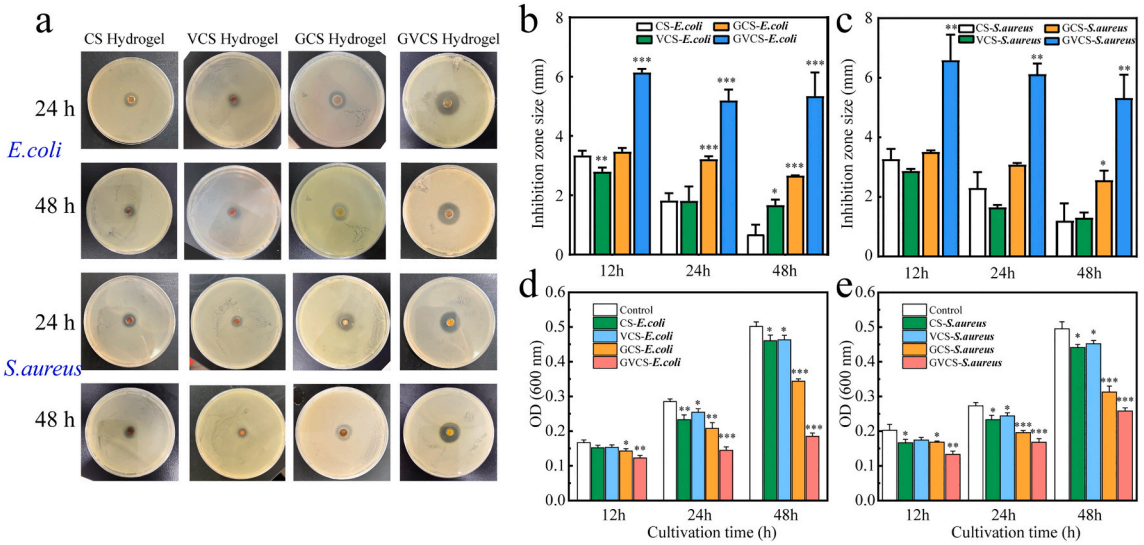

Fig. 5. Inhibition zone pictures of CS, VCS, GCS and GVCS hydrogels against *E. coli* and *S. aureus* (a); Inhibition zone size of hydrogel against *E. coli* (b) and *S. aureus* (c); Sustained antibacterial activity of hydrogels against *E. coli* and *S. aureus* (e). (n = 3, *p < 0.05, **p < 0.01, ***p < 0.001).

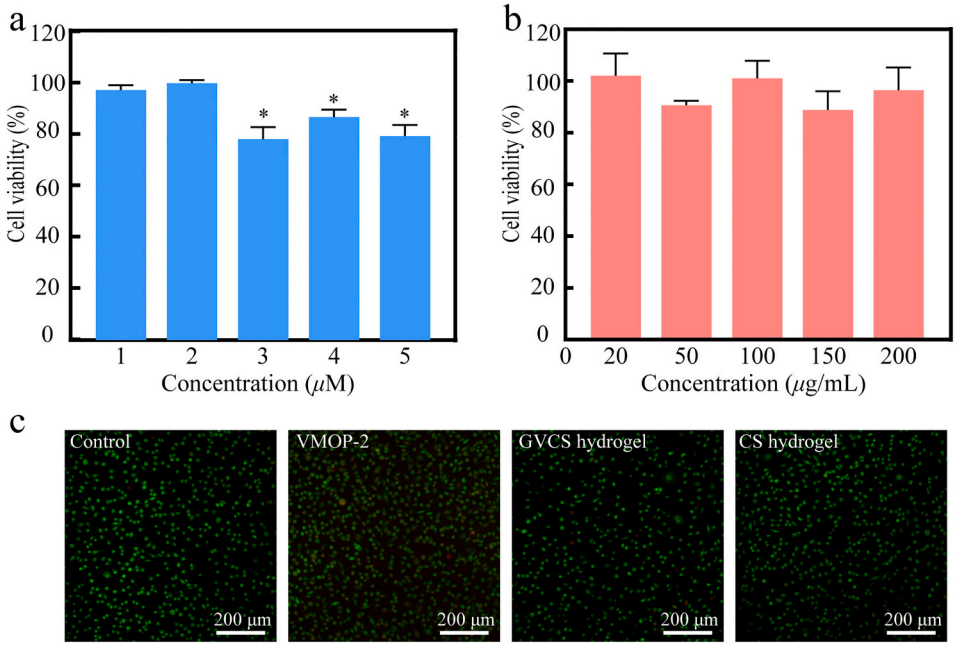

Fig. 6. Cell viability of L929 cells after 48 h incubation with of VMOP-2 (a) and GVCS hydrogel (b); Fluorescent images of L929 cells after treatment with VMOP-2 (5 μM), GVCS (200 μg/mL) and CS hydrogel (200 μg/mL) in comparison with control. (n = 3, *p < 0.05).

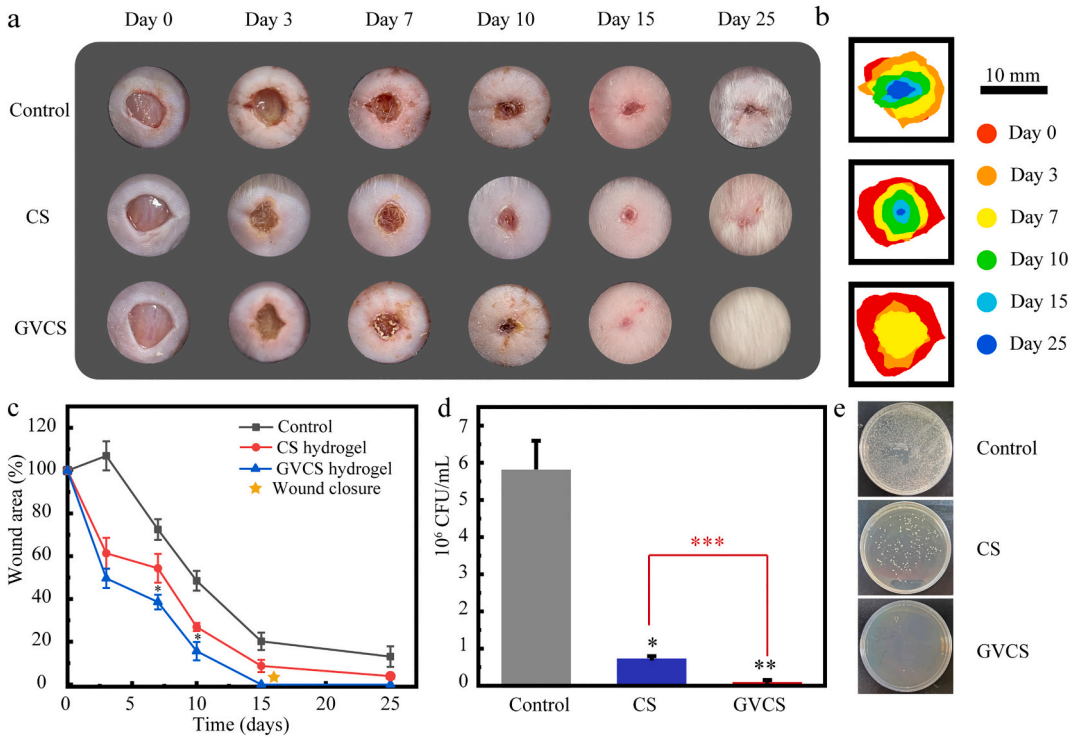

Fig. 7. (a) Photographs of *S. aureus*-infected wounds on mice after treatment at different times; (b–c) Relative wound area of mice after different treatments; (d–e) Colony situation of surviving bacteria in the wound tissue. (n = 3, *p < 0.05, **p < 0.01, ***p < 0.001).

granulation tissues in GVCS group appear more matured and compacted than those in other groups, and more blood vessels (red arrows) are well-distributed around the wound. Faster angiogenesis and good distribution of fibroblasts could promote growth of granulation tissue, leading to faster and better re-epithelialization (Dai et al., 2017). Masson's trichrome staining was used to analyze collagen deposition of skin wound (Fig. 8b). The collagen deposition appears denser and more organized in GVCS group, suggesting that GVCS hydrogel could better promote wound closure.

IHC staining of tumor necrosis factor-α (TNF-α) and VEGF was also performed. All groups show TNF-α expression on day 10 (Fig. 9a), in agreement with high inflammatory phase at the wound. Compared with control and CS groups, GVCS group shows lower TNF-α expression on day 25, suggesting that GVCS group moved quicker from the inflammatory phase to the remodeling phase. In addition, more VEGF expression is observed in GVCS group than control and CS groups

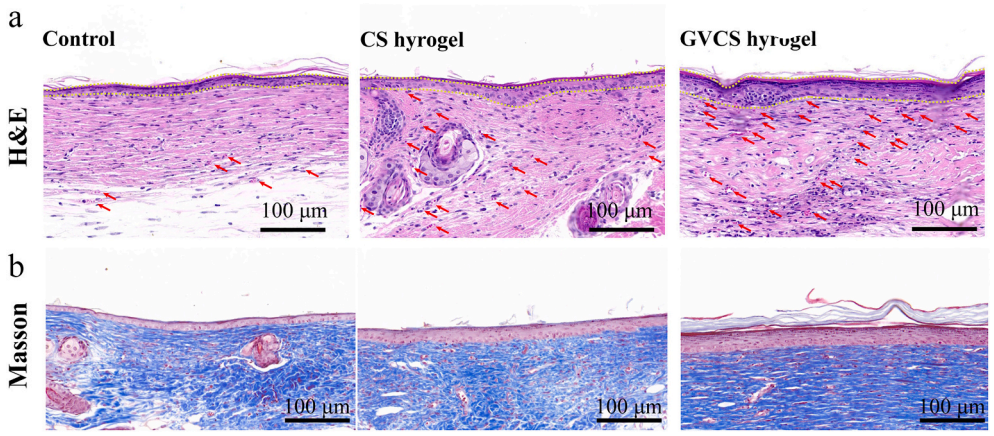

Fig. 8. Histological studies with H&E staining (a) and Masson's trichrome staining (b) of skin tissues.

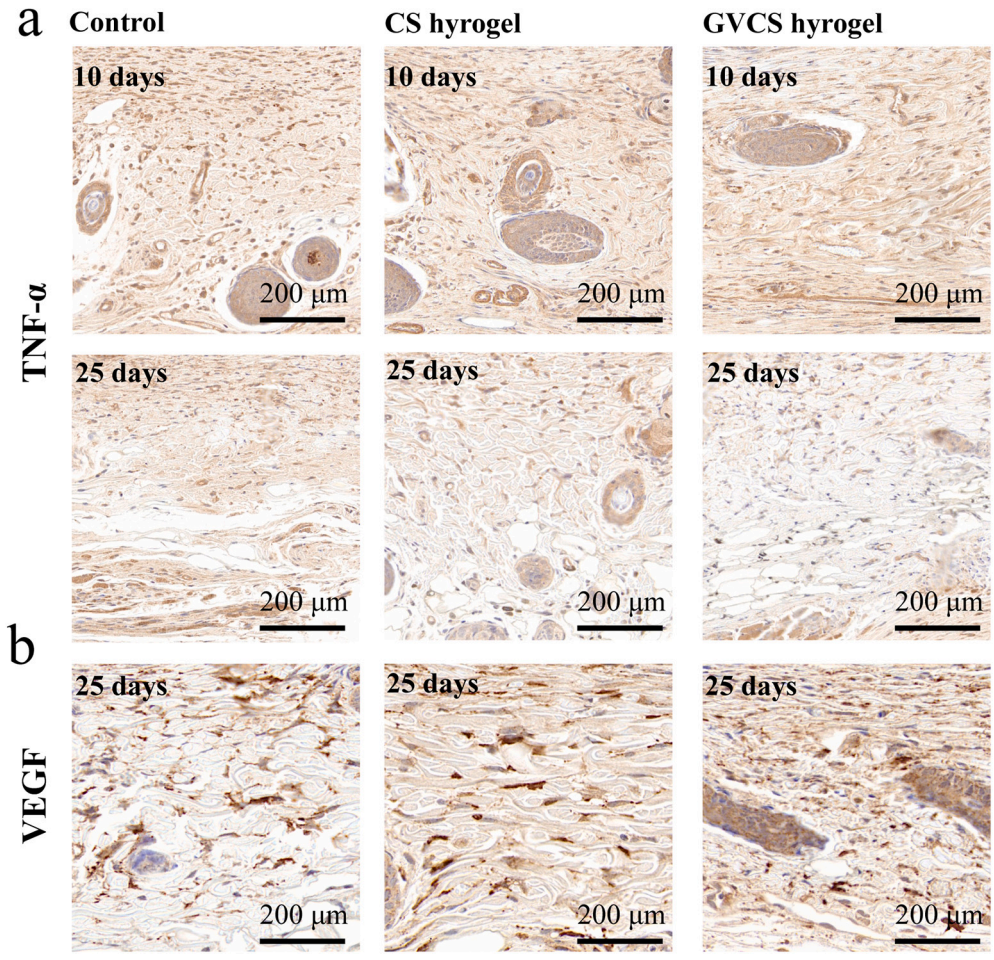

Fig. 9. Immunohistochemical (IHC) staining of TNF-α (a) and VEGF (b).

(Fig. 9b). These findings suggest that GVCS hydrogel may promote wound healing due to inhibited inflammation caused by infection and enhanced angiogenesis in the wound area.

4. Conclusions

A chitosan based MOP/enzyme hybrid hydrogel was synthesized for antibacterial therapy. This system presents a number of advantages compared to currently used hydrogel based wound dressings. First, VMOP-2 can be easily dispersed for the preparation of uniform hybrid hydrogel. Second, •OH radicals are generated by the cascade catalysis of GOx and VMOP-2 as glucose is sequentially converted into H_2O_2 and •OH, which could enhance the antibacterial effect. Third, hybrid hydrogel could consume glucose in wounds and thus prevent the nutrients supply to bacteria, greatly reducing bacterial content in the wound. Thus the hybrid hydrogel exhibits high antibacterial efficiency *in vitro* and wound healing effect *in vivo*. Fourth, chitosan in hybrid hydrogel could accelerate wound healing and improve the treatment

effect. To the best of our knowledge, this is the first report on chitosan based MOP/enzyme hybrid hydrogel for antibacterial therapy. This work could pave the way for antibacterial therapy of MOP-based hybrid hydrogels in clinical applications.

References

Bae, J., Baek, K., Yuan, D., Kim, W., Kim, K., Zhou, H.-C., & Park, J. (2017). Reversible photoreduction of Cu(ii)–coumarin metal–organic polyhedra. *Chemical Communications, 53*(66), 9250–9253.

Bayer, I. S. (2021). A review of sustained drug release studies from nanofiber hydrogels. *Biomedicines, 9*(11), 1612.

Bhattarai, N., Gunn, J., & Zhang, M. (2010). Chitosan-based hydrogels for controlled, localized drug delivery. *Advanced Drug Delivery Reviews, 62*(1), 83–99.

Biesinger, M. C., Lau, L. W. M., Gerson, A. R., & Smart, R. S. C. (2010). Resolving surface chemical states in XPS analysis of first row transition metals, oxides and hydroxides: Sc, Ti, V,Cu and Zn. *Applied Surface Science, 257*(3), 887–898.

Cai, P., Zhang, X., Wang, M., Wu, Y.-L., & Chen, X. (2018). Combinatorial nano–bio interfaces. *ACS Nano, 12*(6), 5078–5084.

Carné-Sánchez, A., Craig, G. A., Larpent, P., Guillerm, V., Urayama, K., Maspoch, D., & Furukawa, S. (2019). A coordinative solubilizer method to fabricate soft porous materials from insoluble metal-organic polyhedra. *Angewandte Chemie International Edition, 58*(19), 6347–6350.

Carné-Sánchez, A., Craig, G. A., Larpent, P., Hirose, T., Higuchi, M., Kitagawa, S. Furukawa, S., … (2018). Self-assembly of metal–organic polyhedra into supramolecular polymers with intrinsic microporosity. *Nature Communications, 9*(1), 1–8.

Chen, L., Qin, Y., Cheng, J., Cheng, Y., Lu, Z., Liu, X.Cao, Q., … (2020). A biocompatible PAA-cu-MOP hydrogel for wound healing. *RSC Advances, 10*(59), 36212–36218.

Cui, Z., Zheng, Z., Lin, L., Si, J., Wang, Q., Peng, X., & Chen, W. (2018). Electrospinning and crosslinking of polyvinyl alcohol/chitosan composite nanofiber for transdermal drug delivery. *Advances in Polymer Technology, 37*(6), 1917–1928.

Dai, X., Liu, J., Zheng, H., Wichmann, J., Hopfner, U., Sudhop, S.Schilling, A. F., … (2017). Nano-formulated curcumin accelerates acute wound healing through Dkk-1-mediated fibroblast mobilization and MCP-1-mediated anti-inflammation. *NPG Asia Materials, 9*(3). e368-e368.

de Lima, H. H. C., da Silva, C. T. P., Kupfer, V. L., de C. Rinaldi, J., Kioshima, E. S., Mandelli, D., & Rinaldi, A. W. (2021). Synthesis of resilient hybrid hydrogels using UiO-66 MOFs and alginate (hydroMOFs) and their effect on mechanical and matter transport properties. *Carbohydrate Polymers, 251*, Article 116977.

Dudek, G., Turczyn, R., & Konieczny, K. (2020). Robust poly(vinyl alcohol) membranes containing chitosan/chitosan derivatives microparticles for pervaporative dehydration of ethanol. *Separation and Purification Technology, 234*, Article 116094.

Eddaoudi, M., Kim, J., Wachter, J., Chae, H., O'Keeffe, M., & Yaghi, O. (2001). Porous metal−organic polyhedra: 25 Å cuboctahedron constructed from 12 Cu2 (CO2) 4 paddle-wheel building blocks. *Journal of the American Chemical Society, 123*(18), 4368–4369.

Gong, F., Yang, N., Wang, Y., Zhuo, M., Zhao, Q., Wang, S.Cheng, L., … (2020). Oxygen-deficient bimetallic oxide FeWOX nanosheets as peroxidase-like nanozyme for sensing cancer via photoacoustic imaging. *Small, 16*(46), 2003496.

Guidolin, K., & Zheng, G. (2019). Nanomedicines lost in translation. *ACS Nano, 13*(12), 13620–13626.

He, J., Shi, M., Liang, Y., & Guo, B. (2020). Conductive adhesive self-healing nanocomposite hydrogel wound dressing for photothermal therapy of infected full-thickness skin wounds. *Chemical Engineering Journal, 394*, Article 124888.

Hu, W. C., Younis, M. R., Zhou, Y., Wang, C., & Xia, X. H. (2020). In situ fabrication of ultrasmall gold nanoparticles/2D MOFs hybrid as nanozyme for antibacterial therapy. *Small, 16*(23), 2000553.

Huang, L., Niu, Y., Li, R., Liu, H., Wang, Y., Xu, G.Xu, Y., … (2019). VOx quantum dots with multienzyme-mimic activities and the application in constructing a three-dimensional (3D) coordinate system for accurate discrimination of the hydrogen peroxide over a broad concentration range. *Analytical Chemistry, 91*(9), 5753–5761.

Kang, Y.-H., Liu, X.-D., Yan, N., Jiang, Y., Liu, X.-Q., Sun, L.-B., & Li, J.-R. (2016). Fabrication of isolated metal–organic polyhedra in confined cavities: Adsorbents/catalysts with unusual dispersity and activity. *Journal of the American Chemical Society, 138*(19), 6099–6102.

Li, D., Chen, T., Zhang, Y., Xu, Y., & Niu, H. (2021). Synergistical starvation and chemo-dynamic therapy for combating multidrug-resistant bacteria and accelerating diabetic wound healing. *Advanced Healthcare Materials, 10*(18), 2100716.

Li, J.-R., & Zhou, H.-C. (2010). Bridging-ligand-substitution strategy for the preparation of metal–organic polyhedra. *Nature Chemistry, 2*(10), 893–898.

Liu, H.-X., Wang, N., Zhao, C., Ji, S., & Li, J.-R. (2018). Membrane materials in the pervaporation separation of aromatic/aliphatic hydrocarbon mixtures — A review. *Chinese Journal of Chemical Engineering, 26*(1), 1–16.

Liu, Y., Zhu, G., Yang, J., Yuan, A., & Shen, X. (2014). Peroxidase-like catalytic activity of Ag3PO4 nanocrystals prepared by a colloidal route. *PLOS ONE, 9*(10). e109158-e109158.

Lu, W., Yuan, D., Yakovenko, A., & Zhou, H.-C. (2011). Surface functionalization of metal–organic polyhedron for homogeneous cyclopropanation catalysis. *Chemical Communications, 47*(17), 4968–4970.

Martínez-Mejía, G., Vázquez-Torres, N. A., Castell-Rodríguez, A., del Río, J. M., Corea, M., & Jiménez-Juárez, R. (2019). Synthesis of new chitosan-glutaraldehyde scaffolds for tissue engineering using Schiff reactions. *Colloids and Surfaces A: Physicochemical and Engineering Aspects, 579*, Article 123658.

Ming, F., Hou, J., Huo, D., Zhou, J., Yang, M., Shen, C.Hou, C., … (2019). Copper-based metal–organic framework nanoparticles for sensitive fluorescence detection of ferric ions. *Analytical Methods, 11*(34), 4382–4389.

Natalio, F., André, R., Hartog, A. F., Stoll, B., Jochum, K. P., Wever, R., & Tremel, W. (2012). Vanadium pentoxide nanoparticles mimic vanadium haloperoxidases and thwart biofilm formation. *Nature Nanotechnology, 7*(8), 530–535.

Nematidil, N., Sadeghi, M., Nezami, S., & Sadeghi, H. (2019). Synthesis and characterization of Schiff-base based chitosan-g-glutaraldehyde/NaMMTNPs-APTES for removal Pb2+ and Hg2+ ions. *Carbohydrate Polymers, 222*, Article 114971.

Ou, Q., Huang, K., Fu, C., Huang, C., Fang, Y., Gu, Z.Wang, Y., … (2020). Nanosilver-incorporated halloysite nanotubes/gelatin methacrylate hybrid hydrogel with osteoimmunomodulatory and antibacterial activity for bone regeneration. *Chemical Engineering Journal, 382*, Article 123019.

Patrulea, V., Ostafe, V., Borchard, G., & Jordan, O. (2015). Chitosan as a starting material for wound healing applications. *European Journal of Pharmaceutics and Biopharmaceutics, 97*, 417–426.

Peng, L., Yang, X., Wang, S., Chan, Y. K., Chen, Y., et al. (2022). Bimetal metal-organic framework domino micro-reactor for synergistic antibacterial starvation/chemodynamic therapy and robust wound healing. *Nanoscale, 14*(5), 2052–2064.

Qin, Y., Chen, L.-L., Pu, W., Liu, P., Liu, S.-X., Li, Y.Cao, Q.-E., … (2019). A hydrogel directly assembled from a copper metal–organic polyhedron for antimicrobial application. *Chemical Communications, 55*(15), 2206–2209.

Qu, J., Zhao, X., Liang, Y., Xu, Y., Ma, P. X., & Guo, B. (2019). Degradable conductive injectable hydrogels as novel antibacterial, anti-oxidant wound dressings for wound healing. *Chemical Engineering Journal, 362*, 548–560.

Reddy, M., Jugnee, N., El Laboudi, A., Spanudakis, E., Anantharaja, S., & Oliver, N. (2018). A randomized controlled pilot study of continuous glucose monitoring and flash glucose monitoring in people with type 1 diabetes and impaired awareness of hypoglycaemia. *Diabetic Medicine, 35*(4), 483–490.

Sun, H., Gao, N., Dong, K., Ren, J., & Qu, X. (2014). Graphene quantum dots-band-aids used for wound disinfection. *ACS Nano, 8*(6), 6202–6210.

Tao, B., Lin, C., Deng, Y., Yuan, Z., Shen, X., Chen, M.Cai, K., … (2019). Copper-nanoparticle-embedded hydrogel for killing bacteria and promoting wound healing with photothermal therapy. *Journal of Materials Chemistry B, 7*(15), 2534–2548.

Wang, G., Lu, G., Ao, Q., Gong, Y., & Zhang, X. (2009). Preparation of cross-linked carboxymethyl chitosan for repairing sciatic nerve injury in rats. *Biotechnology Letters, 32*(1), 59.

Wang, L., Zhang, L., Qiu, S., Liu, C., Zhang, P., Yin, L., & Chen, F. (2019). Rheological properties and structural characteristics of arabinoxylan hydrogels prepared from three wheat bran sources. *Journal of Cereal Science, 88*, 79–86.

Wang, P., Peng, L., Lin, J., Li, Y., Luo, Q., Jiang, S.Liu, J., … (2021). Enzyme hybrid virus-like hollow mesoporous CuO adhesive hydrogel spray through glucose-activated cascade reaction to efficiently promote diabetic wound healing. *Chemical Engineering Journal, 415*, Article 128901.

Wang, X., Zhou, X., Yang, K., Li, Q., Wan, R., Hu, G.Gu, H., … (2021). Peroxidase-and UV-triggered oxidase mimetic activities of the UiO-66-NH 2/chitosan composite membrane for antibacterial properties. *Biomaterials Science, 9*(7), 2647–2657.

Wu, F., Meng, G., He, J., Wu, Y., Wu, F., & Gu, Z. (2014). Antibiotic-loaded chitosan hydrogel with superior dual functions: Antibacterial efficacy and osteoblastic cell responses. *ACS Applied Materials & Interfaces, 6*(13), 10005–10013.

Xiao, J., Chen, S., Yi, J., Zhang, H. F., & Ameer, G. A. (2017). A cooperative copper metal-organic framework-hydrogel system improves wound healing in diabetes. *Advanced Functional Materials, 27*(1), 1604872.

Xue, Z., Li, Y., Zhang, Y., Geng, W., Jia, B., Tang, J.Su, C.-Y., … (2018). Modulating electronic structure of metal-organic framework for efficient electrocatalytic oxygen evolution. *Advanced Energy Materials, 8*(29), 1801564.

Yang, F., Zhao, J., Koshut, W. J., Watt, J., Riboh, J. C., Gall, K., & Wiley, B. J. (2020). A synthetic hydrogel composite with the mechanical behavior and durability of cartilage. *Advanced Functional Materials, 30*(36), 2003451.

Yao, S., Chi, J., Wang, Y., Zhao, Y., Luo, Y., & Wang, Y. (2021). Zn-MOF encapsulated antibacterial and degradable microneedles array for promoting wound healing. *Advanced Healthcare Materials, 10*(12), 2100056.

Zeb, A., Xie, X., Yousaf, A. B., Imran, M., Wen, T., Wang, Z.Xu, A.-W., … (2016). Highly efficient Fenton and enzyme-mimetic activities of mixed-phase VO x nanoflakes. *ACS Applied Materials & Interfaces, 8*(44), 30126–30132.

Zhang, L., Liu, Z., Deng, Q., Sang, Y., Dong, K., Ren, J., & Qu, X. (2021). Nature-inspired construction of MOF@COF nanozyme with active sites in tailored microenvironment and pseudopodia-like surface for enhanced bacterial inhibition. *Angewandte Chemie International Edition, 60*(7), 3469–3474.

Zhang, Y., Tao, L., Li, S., & Wei, Y. (2011). Synthesis of multiresponsive and dynamic chitosan-based hydrogels for controlled release of bioactive molecules. *Biomacromolecules, 12*(8), 2894–2901.

Zhang, Y.-T., Wang, X.-L., Zhou, E.-L., Wu, X.-S., Song, B.-Q., Shao, K.-Z., & Su, Z.-M. (2016a). Polyoxovanadate-based organic–inorganic hybrids: From V5O9Cl clusters to nanosized octahedral cages. *Dalton Transactions, 45*(9), 3698–3701.

Zhang, Y.-T., Wang, X.-L., Zhou, E.-L., Wu, X.-S., Song, B.-Q., Shao, K.-Z., & Su, Z.-M. (2016b). Polyoxovanadate-based organic–inorganic hybrids: From V 5 O 9 cl clusters to nanosized octahedral cages. *Dalton Transactions, 45*(9), 3698–3701.